

1 **Understanding the geodetic signature of large aquifer**
2 **systems: Example of the Ozark Plateaus in Central**
3 **United States**

4 **Stacy Larochele¹, Kristel Chanard^{2,3}, Luce Fleitout⁴, Jérôme Fortin⁵, Adriano**
5 **Gualandi^{1,6}, Laurent Longuevergne⁷, Paul Rebischung^{2,3}, Sophie Violette^{4,8},**
6 **and Jean-Philippe Avouac¹**

7 ¹Geological and Planetary Sciences, California Institute of Technology, Pasadena, California, USA

8 ²Université de Paris, Institut de physique du globe de Paris, CNRS, IGN, Paris, France

9 ³ENSG-Géomatique, IGN, Marne-la-Vallée, France

10 ⁴Laboratoire de Géologie, École Normale Supérieure, Université PSL, CNRS, Paris, France

11 ⁵University PSL, CNRS UMR 8538, Paris, France

12 ⁶Istituto Nazionale di Geofisica e Vulcanologia, Bologna, Italy

13 ⁷Univ Rennes, CNRS, Geosciences Rennes - UMR 6118, F-35000 Rennes, France

14 ⁸Sorbonne University, UFR.918, Paris, France

15 **Key Points:**

- 16 • We characterize seasonal and multiannual groundwater fluctuations with an In-
17 dependent Component Analysis.
18 • We separate and model the hydrological loading and poroelastic deformation fields
19 captured by GNSS.
20 • We infer relatively low elastic moduli from the extracted poroelastic displacements
21 and groundwater fluctuations.

Corresponding author: Stacy Larochele, stacy.larochele@caltech.edu

22 **Abstract**

23 The continuous redistribution of water mass involved in the hydrologic cycle leads
 24 to deformation of the solid Earth. On a global scale, this deformation is well explained
 25 by redistribution in surface loading and can be quantified to first order with space-based
 26 gravimetric and geodetic measurements. At the regional scale, however, aquifer systems
 27 also undergo poroelastic deformation in response to groundwater fluctuations. Disentan-
 28 tling these related but distinct 3D deformation fields from geodetic time series is essen-
 29 tial to accurately invert for changes in continental water mass, to understand the me-
 30 chanical response of aquifers to internal pressure changes as well as to correct time se-
 31 ries for these known effects. Here, we demonstrate a methodology to accomplish this task
 32 by considering the example of the well-instrumented Ozark Plateaus Aquifer System (OPAS)
 33 in central United States. We begin by characterizing the most important sources of signal
 34 in the spatially heterogeneous groundwater level dataset using an Independent Com-
 35 ponent Analysis. Then, to estimate the associated poroelastic displacements, we project
 36 geodetic time series corrected for surface loading effects onto orthogonalized versions of
 37 the groundwater temporal functions. We interpret the extracted displacements in light
 38 of analytical solutions and a 2D model relating groundwater level variations to surface
 39 displacements. In particular, the relatively low estimates of elastic moduli inferred from
 40 the poroelastic displacements and groundwater fluctuations may be indicative of surficial
 41 layers with a high fracture density. Our findings suggest that OPAS undergoes signifi-
 42 cant poroelastic deformation, including highly heterogeneous horizontal poroelastic
 43 displacements.

44 **1 Introduction**

45 Hydrological processes occurring at the surface of the Earth redistribute continen-
 46 tal water mass and deform the solid Earth. The resulting, primarily seasonal, deforma-
 47 tion can be measured with space-based geodetic techniques such as GNSS (Global Nav-
 48 igation Satellite System)(Blewitt et al., 2001; van Dam et al., 2001; Dong et al., 2002).
 49 It is thus possible to infer fluctuations in continental water storage from GNSS time se-
 50 ries (Ouellette et al., 2013; Argus et al., 2014, 2017; Borsa et al., 2014; Fu et al., 2015;
 51 Adusumilli et al., 2019; Ferreira et al., 2019) assuming that the regional deformation field
 52 induced by hydrology can be separated from other geodetic signals and/or systematic
 53 errors (Chanard et al., 2020). Such regional-scale constraints on hydrological fluctuations
 54 help bridge the gap between *in situ* measurements (e.g., groundwater monitoring wells,
 55 stream gauges) and continental-scale observations from the Gravity Recovery and Cli-
 56 mate Experiment (GRACE) mission (Tapley et al., 2004).

57 However, at a global scale, seasonal signals in geodetic time series are not entirely
 58 explained by hydrological loads measured by GRACE (Chanard et al., 2018). Additional
 59 deformation mechanisms related to groundwater and temperature variations are thought
 60 to explain a significant fraction of this seasonal variance (Tsai, 2011). In particular, aquifer
 61 basins - which store roughly 30% of Earth’s freshwater reserves (Shiklomanov, 1993) -
 62 are prone to poroelastic swelling in addition to hydrological loading (Wang, 2000). A re-
 63 duction in total water storage translates to a release of load which leads to uplift and
 64 horizontal displacements pointing away from the released load (Boussinesq, 1885; Ver-
 65 ruijt, 2009) (Figure 1A). A reduction in groundwater storage, on the other hand, also
 66 lowers pore pressure within the aquifer, which leads to subsidence and radially inward
 67 displacements as support of the overburden weight is transferred from the pore fluid to
 68 the compressible porous rock (King et al., 2007; Wisely & Schmidt, 2010; Galloway &
 69 Burbey, 2011) (Figure 1B).

70 Separating the contributions of hydrological loading and poroelasticity in geode-
 71 tic time series is crucial to better understand the physics of either deformation processes
 72 and quantify fluctuations in total water storage. Extracting the poroelastic deformation

73 field has direct implications for inferring, at the field scale, the hydromechanical prop-
 74 erties of aquifer systems which are tightly linked to hydrodynamical properties. Indeed,
 75 surface deformation provides information about internal aquifer processes which are gen-
 76 erally not accessible otherwise. Such insight could improve the representation of ground-
 77 water within global and regional hydrological models and hence strengthen their predic-
 78 tive ability (Gleeson et al., 2021). Estimates of effective elastic moduli obtained through
 79 geodesy also provide measurements at a scale and loading rate (i.e., quasi-static) rele-
 80 vant for geohydrologic processes and complementary to those obtained through seismol-
 81 ogy and laboratory experiments (Carlson et al., 2020). Beyond hydrological applications,
 82 characterizing the seasonal content of geodetic time series is also essential to isolate the
 83 deformation associated with tectonic processes (Michel et al., 2019; Vergnolle et al., 2010)
 84 and to investigate the response of seismicity to seasonal loading (Bettinelli et al., 2008;
 85 Craig et al., 2017; C. W. Johnson et al., 2017).

86 A number of studies, mostly using Interferometric Synthetic Aperture Radar (In-
 87 SAR), have demonstrated the feasibility of documenting aquifer dynamics and inferring
 88 their mechanical properties based on remote sensing measurements of surface deforma-
 89 tion and *in situ* measurements of groundwater levels (Amelung et al., 1999; Bell et al.,
 90 2008; Wisely & Schmidt, 2010; Galloway & Burbey, 2011; Chaussard et al., 2014, 2017;
 91 Miller et al., 2017; Ojha et al., 2018; Riel et al., 2018; Alghamdi et al., 2020; Hu & Bürgmann,
 92 2020; Gualandi & Liu, 2021). Most of these studies focused on aquifer basins where the
 93 poroelastic response dominates the local deformation field. At a regional scale, however,
 94 both deformation fields vary spatially and are not easily separated given the codepen-
 95 dency of these deformation processes.

96 Here, we propose a methodology to isolate the poroelastic contribution in GNSS
 97 time series with the help of GRACE and groundwater level measurements. Focusing on
 98 GNSS data as opposed to InSAR provides (1) a complementary set of geodetic obser-
 99 vations with different systematic errors, (2) the opportunity to study larger aquifer sys-
 100 tems at which InSAR processing becomes challenging and (3) a means to correct for known
 101 hydrological effects in GNSS time series extensively used in tectonic studies. Indeed, GNSS
 102 provides insight into the 3D surface deformation field complementary to InSAR, partic-
 103 ularly when it comes to horizontal displacements. This is important because, as we em-
 104 phasize in this work, horizontal and vertical deformation fields arising from different mech-
 105 anisms can have distinct spatial signatures.

106 In this manuscript, we first introduce the geohydrological setting and data sets of
 107 our test region: the Ozark Plateaus Aquifer System (OPAS) in central United States.
 108 We selected this particular aquifer system to carry out our investigation because of its
 109 relative tectonic quiescence (Craig & Calais, 2014; Calais et al., 2016), data availabil-
 110 ity and the existing geohydrological literature in the region (e.g., Imes & Emmett, 1994;
 111 Hays et al., 2016; Westerman et al., 2016; Knierim et al., 2017). We then extract the de-
 112 formation signals related to hydrology using GNSS time series, a GRACE-derived load-
 113 ing model and groundwater level data with a statistical Blind Source Separation (BSS)
 114 technique. We compare the extracted horizontal displacements with the predictions of
 115 a 2D analytical poroelastic model and infer elastic properties of the aquifer layers from
 116 the vertical poroelastic displacements and groundwater level variations. We conclude with
 117 a discussion of the merits and limitations of the methodology.

118 2 Regional setting and data sets

119 2.1 The Ozark Plateaus Aquifer System (OPAS)

120 OPAS is a large system of aquifers and confining units in the Mississippi River basin
 121 in central United States (Figure 2). The system is bounded by the Mississippi River and
 122 its alluvial plain, the Missouri River and Arkansas River to the east, north and south,

123 respectively, and by a saline to freshwater transition zone to the west (Imes & Emmett,
 124 1994) (Figure 2A). Although it is a significant source of water for agricultural and pub-
 125 lic supply in the region, groundwater use in OPAS represents a relatively small portion
 126 of the hydrologic budget – about 2% of aquifer recharge (Hays et al., 2016). Most ground-
 127 water recharge flows laterally, feeding other aquifers and sustaining streams, lakes and
 128 wetlands (Hays et al., 2016). Nonetheless, groundwater pumping does cause localized
 129 cones of depression around certain urban areas such as Springfield, Missouri (Imes, 1989).

130 OPAS is composed of interbedded layers of carbonate and clastic deposits around
 131 the topographic high Ozark dome (Hays et al., 2016; Westerman et al., 2016). The sys-
 132 tem is underlain by a basement confining unit which outcrops at the Ozark dome in east-
 133 central Missouri (Figure 2AC). The Ozark aquifer system (OAS) – the most important
 134 water-bearing unit of the system – crops out at the center of the system and is other-
 135 wise overlaid by the Springfield Plateau aquifer system (SPAS) and/or the Western In-
 136 terior Plains confining system (WIPCS). North of the Missouri - Arkansas border, carbonate-
 137 rich units such as SPAS and OAS present rich karst features (Hays et al., 2016).

138 Other aquifer systems surrounding OPAS are also shown in Figure 2. The Missis-
 139 sippi Embayment Aquifer System and the shallower Mississippi River Valley Aquifer south-
 140 east of OPAS supply much of the irrigation water for the agriculture-intensive region (Hart
 141 et al., 2008). The Mississippian Aquifers and glacial deposits from the Laurentide Ice
 142 Sheet occupy the north and northeastern boundaries of the study area (Bayless et al.,
 143 2017).

144 **2.2 Data sets**

145 *2.2.1 Groundwater level time series*

146 Groundwater monitoring wells (i.e., piezometers) record the temporal evolution of
 147 hydraulic head at a given depth. In this study, we take advantage of the piezometric net-
 148 work maintained by the United States Geological Survey which provides daily observa-
 149 tions of water level depth (USGS Water Services; <https://waterservices.usgs.gov>). Of the
 150 312 wells in the study area, we retain the 167 sites with 60% or more data completeness
 151 during the 2007 to 2017 timespan and further exclude seven stations classified as anomalous
 152 after visual inspection (Figure S1). For example, two time series with a typical ground-
 153 water pumping signature (Figure S1) are excluded from the analysis because these sig-
 154 nals are expected to be very local (tens of meters) - as they represent the aquifer response
 155 to local forcings - and to bias the analysis due to their large amplitudes. We subtract
 156 the altitude at each well location to obtain the hydraulic head, detrend the time series
 157 and compute monthly averages to facilitate comparison with the other data sets used
 158 in this study. The positions of the 160 selected wells are shown in Figure 3A and exam-
 159 ples of retained time series are presented in Figure 3B. They present seasonal and multi-
 160 annual water level oscillations from a few to tens of meters in amplitude.

161 *2.2.2 GRACE-derived displacement time series*

162 GRACE satellites monitor space and time variations in Earth’s gravity field from
 163 which changes in continental water storage can be inferred and expressed in units of equiv-
 164 alent water height (EWH). At the global scale, GRACE-based models have been shown
 165 to better explain the seasonal signals in GNSS datasets than hydrology-based models
 166 (Li et al., 2016). Here, we make use of the Level 2 (Release 06) spherical harmonics GRACE
 167 solution provided by the Center for Space Research (CSR) (Bettadpur, 2018; GRACE,
 168 2018) and DDK5-filtered to minimize north-south striping noise (Kusche et al., 2009).
 169 We add back the atmospheric and non-tidal oceanic contributions as these effects are not
 170 corrected in the GNSS data set and detrend the resulting time series. The colormap in
 171 Figure 3A shows the average annual EWH peak-to-peak amplitudes observed during the

172 2007 to 2017 timespan and reveals an important large-scale NW to SE gradient in re-
 173 gional water storage changes, with higher amplitudes concentrated around the Missis-
 174 sippi Alluvial Valley.

175 To enable direct comparison with the GNSS displacement time series, we compute
 176 the deformation expected from GRACE-inferred surface loads at the GNSS sites using
 177 a spherical elastic layered Earth model based on the Love number formalism (Farrell,
 178 1972; Chanard et al., 2018). Examples of these predicted time series are compared to
 179 the corresponding GNSS measurements in Figure S2.

180 **2.2.3 GNSS displacement time series**

181 GNSS tracks the vertical and horizontal displacements of geodetic monuments an-
 182 chored a few meters below the ground surface (or on top of buildings for fewer than 15%
 183 of stations). In this analysis, we start from the time series processed by the Nevada Geode-
 184 tic Laboratory and expressed in the IGS14 reference frame (International GNSS Service),
 185 based on the latest release of the International Terrestrial Reference Frame (ITRF2014),
 186 (Altamimi et al., 2016; Blewitt et al., 2018, <http://geodesy.unr.edu>). Of the 315 sta-
 187 tions located in the study area which is delimited by longitudes -96° to -89° and latitudes
 188 34.5° to 40.5° , we retain the 92 stations with at least 60% of daily data between 2007
 189 and 2017. After visual inspection, six additional stations (CVMS, MOGF, MOMK, MOSI,
 190 NWCC, and SAL5) are discarded due to spurious large amplitude signals. The positions
 191 of the remaining 86 stations are shown in Figures 3A and S3.

192 For each time series, we fit a trajectory model (Bevis & Brown, 2014) with a lin-
 193 ear trend, annual and semi-annual terms and step functions to account for material changes
 194 and potential coseismic displacements (<http://geodesy.unr.edu/NGLStationPages/steps.txt>)
 195 as well as visually obvious offsets. We subtract the best-fit linear trend and step func-
 196 tions from the time series but do not correct for the periodic terms. Next, we identify
 197 and eliminate outliers defined as points that exceed three times the average deviation
 198 from the 90-day median for any of the three directions (east, north, vertical). The time
 199 series are then monthly averaged to match the GRACE temporal resolution. Finally, the
 200 spherical harmonic degree-1 deformation field is estimated from a global network of 1150
 201 GNSS stations and subtracted from retained GNSS time series to allow for a direct com-
 202 parison with GRACE observations which do not capture degree-1 mass changes (Cha-
 203 nard et al., 2018). Examples of the resulting time series are provided in Figure S2.

204 **3 Fluctuations in groundwater levels**

205 The first step towards extracting poroelastic signals from our GNSS dataset is to
 206 characterize the groundwater fluctuations responsible for the deformation. This requires
 207 some form of spatial interpolation since piezometers only probe groundwater levels at
 208 discrete points in space and are generally not co-located with GNSS stations. We de-
 209 termine that directly interpolating between the piezometric sensors is not warranted in
 210 this case given the heterogeneous nature of aquifers and the variable depth of wells (Fig-
 211 ure 3). For example, neighboring piezometers GW1 and GW2 in Figure 3B reveal very
 212 different temporal signatures. On the other hand, GW2 and GW3 - which are over 200
 213 km apart - have highly correlated time series. Groundwater fluctuations at GW4 also
 214 correlate with GW2 and GW3 but are of much higher amplitude. The groundwater dataset
 215 thus contains both regional- and local-scale signals with peak-to-peak amplitudes that
 216 span two orders of magnitude (~ 0.5 to 50 m).

217 **3.1 Extracting groundwater signals with ICA**

218 In light of these observations, we perform an Independent Component Analysis (ICA)
 219 on the groundwater dataset to extract the main modes of variability before proceeding

with the spatial interpolation. ICA algorithms seek to recover the statistically independent sources of signal assumed to generate the linearly mixed time series at each sensor (Roberts & Everson, 2001). In particular, variational Bayesian ICA (vbICA) (Choudrey, 2002) has been shown to perform well to recover geophysical signals (e.g., postseismic, hydrology-induced and common mode error) from synthetic and real GNSS data sets (Gualandi et al., 2016; Larochelle et al., 2018). Once an independent component (IC) - i.e. a source of signal - i is isolated, it can be expressed with space and time vectors as $IC_i = U_i S_i V_i^T$ where U_i is a normalized spatial distribution, S_i is a weighting factor and V_i is a normalized temporal function.

Figure 4 shows the temporal functions (A), weighting factors (A) and spatial distributions (B-D) obtained from a 3 components vbICA of the groundwater dataset. We use a triangulation-based natural neighbor algorithm (MATLAB, 2017) to interpolate the spatial distributions from the discrete data points (Figure 4B-D). We choose to limit our analysis to 3 components since analyses with more components (e.g., see Figure S4 for a 5 components analysis) yield similar IC1-3 and additional lower-amplitude ICs with spurious temporal functions that only explain a limited portion of data variance. The retained temporal functions all display a mix of multiannual and seasonal frequencies.

IC_1 , the component which explains the greatest share of data variance, has an overall positive spatial distribution and is observed at almost all wells including those outside OPAS (Figure 4B). This spatial distribution is indicative of a regional income of water linked to recharge processes (Longuevergne et al., 2007). The large fluctuations occurring in southern Missouri (e.g., at station GW4 (Figure 3)) are likely linked to the high storage capacity of thick limestone layers with limited karstification (Figure 4B). Figure 5 also reveals a first order spatial correlation between sinkhole density, which suggests a higher ability to recharge the aquifer system, and wells with high $S_1 U_1$ values. IC_2 and IC_3 represent seasonal and multi-annual signals with different phases than IC_1 and exhibit heterogeneous spatial distributions with positive and negative values (Figure 4CD). These components probably compensate for local deviations from the regional behavior due to the delayed response of deeper aquifers, differing recharge and discharge mechanisms and groundwater pumping.

3.2 Comparing regional-scale hydrological signals across datasets

Given that IC_1 spans the entire study region, we expect to find a similar signal in the GRACE dataset. Performing a vbICA on the GRACE-predicted vertical displacements, the temporal function of the first and most important component indeed correlates very well with V_1^{GW} ($\rho = 0.81$) (Figure 6A). Downward motion occurs concurrently with rising groundwater levels because GRACE-derived vertical displacements reflect storage changes which drives the elastic deformation (Figure 1A), but not the poroelastic deformation (Figure 1B). The associated spatial response (Figure 6B) reflects the northwest to southwest gradient of surface loading.

By contrast, GNSS vertical time series should comprise both deformation fields. Performing a similar analysis on the GNSS dataset results in a lower but still significant correlation - $\rho = 0.52$ - with V_1^{GW} (Figure 6A). Note that a significant portion of GNSS stations sitting on top of OPAS were not installed until 2010 or 2011 as indicated by the grey shading in Figure 6A. Although the GNSS spatial distribution displays the same overall gradient as the GRACE-derived model with generally higher amplitudes around the Mississippi Alluvial Valley, the response is much more heterogeneous (Figure 6B).

This comparison exercise demonstrates that the dominant temporal functions of all three datasets are in phase on a monthly timescale. This is consistent with a relatively uniform regional recharge of the aquifer system (Figure 4B) and with the system's karstic nature which allows for rapid communication between surface water and groundwater (Hays et al., 2016), suggesting that the aquifer global behavior can be considered

271 as unconfined. Although OPAS is a complex aquifer system with both confined and un-
 272 confined units (Figure 3A), and that different hydrogeologic processes might interact to
 273 generate surface deformation, in this work we assume that OPAS is an unconfined sys-
 274 tem.

275 Note that we do not rely on ICA to separate the elastic loading and poroelastic sig-
 276 nals from GNSS time series because the temporal variations in groundwater and total
 277 water storage (derived from GRACE) are highly correlated (Figure 6A) and hence not
 278 statistically independent in this case. ICA algorithms might be better able to accom-
 279 plish this task in other contexts where groundwater levels are controlled by anthropogenic
 280 pumping as opposed to background hydrology.

281 4 Poroelastic deformation

282 4.1 Elastic loading vs poroelastic eigenstrain: Analytical solutions for 283 surface displacements

284 To gain intuition about the elastic and poroelastic deformation fields we expect to
 285 find in the vicinity of an unconfined aquifer, we first develop and compare analytical so-
 286 lutions for surface displacements associated with the simple disk scenarios in an elastic
 287 half-space shown in Figure 1. We then extend the poroelastic solution to an arbitrary
 288 2D loading distribution which we use to predict horizontal poroelastic displacements in
 289 Section 4.4.

290 4.1.1 Disk loading of an elastic half-space

291 Figure 1A shows a disk load of radius a and uniform pressure P at the surface of
 292 an elastic half-space with Young's modulus E_{deep} , representative of surface hydrologi-
 293 cal loading. The corresponding vertical and horizontal surface displacements were de-
 294 rived by Johnson (1987) and Verruijt (2009) as:

$$295 \quad u_z(r) = \begin{cases} -\frac{4(1-\nu^2)}{\pi E_{deep}} Pa \mathcal{E}\left(\frac{r^2}{a^2}\right), & r \leq a \\ -\frac{4(1-\nu^2)}{\pi E_{deep}} Pr \left(\mathcal{E}\left(\frac{a^2}{r^2}\right) - \left(1 - \frac{a^2}{r^2}\right) \mathcal{K}\left(\frac{a^2}{r^2}\right) \right), & r > a \end{cases} \quad (1)$$

$$296 \quad u_r(r) = \begin{cases} -\frac{(1-2\nu)(1+\nu)}{2E_{deep}} Pr, & r \leq a \\ -\frac{(1-2\nu)(1+\nu)}{2E_{deep}} P \frac{a^2}{r}, & r > a \end{cases} \quad (2)$$

297 where $u_z(r)$ and $u_r(r)$ are the vertical and horizontal displacements as a function of ra-
 298 dial distance r and \mathcal{K} and \mathcal{E} are the complete elliptic integral of the first and second kind,
 299 respectively.

300 Figure 7A shows the deformation resulting from 100 km and 250 km-radius disks
 301 uniformly loaded with 150 mm of water, representative of OPAS's spatial extent and EWH
 302 variations derived from GRACE. Both the vertical and horizontal displacements extend
 303 beyond the loaded region with the maximum vertical and horizontal displacements oc-
 304 ccurring at the center of the disk and at the load boundary, respectively. Note that the
 amplitude of deformation depends on the spatial wavelength of the load: Displacements
 grow with increasing disk radius.

305 4.1.2 Poroelastic eigenstrain in a disk within an elastic half-space

306 Poroelastic deformation arises from dilational eigenstrains (Mura, 1982) associated
 307 with changes in pore pressure, analogous to thermoelastic deformation resulting from
 308 changes in temperature. Eigenstrains refer to internal strains which, in the absence of

external stresses resisting them, would lead to isotropic expansion or contraction of the body. In the poroelastic case, eigenstrains are related to changes in pore pressure, Δp , and hence in groundwater level, Δh , as:

$$\varepsilon_{eig} = \frac{\beta \Delta p (1 - 2\nu)}{E_{surf}} = \frac{\beta \rho g \Delta h (1 - 2\nu)}{E_{surf}} \quad (3)$$

where β , ν and E_{surf} are the Biot-Willis coefficient, Poisson's ratio and Young's modulus of the aquifer layers, respectively, while ρ is water density and g is the gravitational acceleration.

Given the relatively high hydraulic conductivity of karstified sedimentary rocks (Domenico & Schwartz, 1998; Hays et al., 2016), in this work we assume that there is no significant time delay between changes in pore pressure and the resulting deformation. We also assume that deformation is entirely elastic and neglect permanent deformation as clay minerals often responsible for inelastic processes are seldom found in OPAS (Westerman et al., 2016).

Linear elastic constitutive equations accounting for eigenstrains are as follows (Wang, 2000):

$$\varepsilon_{zz} = \frac{1}{E_{surf}} [(1 + \nu)\sigma_{zz} - \nu(\sigma_{rr} + \sigma_{\theta\theta} + \sigma_{zz})] + \varepsilon_{eig} \quad (4)$$

$$\varepsilon_{rr} = \frac{1}{E_{surf}} [(1 + \nu)\sigma_{rr} - \nu(\sigma_{rr} + \sigma_{\theta\theta} + \sigma_{zz})] + \varepsilon_{eig} \quad (5)$$

$$\varepsilon_{\theta\theta} = \frac{1}{E_{surf}} [(1 + \nu)\sigma_{\theta\theta} - \nu(\sigma_{rr} + \sigma_{\theta\theta} + \sigma_{zz})] + \varepsilon_{eig} \quad (6)$$

Given that lateral motion is restrained by the elastic medium below, it can be shown that horizontal strains within the aquifer layers, ε_{rr} and $\varepsilon_{\theta\theta}$, are negligible compared to ε_{eig} (Fleitout & Chanard, 2018). Under this assumption, lateral stresses, σ_{rr} and $\sigma_{\theta\theta}$, can be approximated as:

$$\sigma_{rr} = \sigma_{\theta\theta} = \frac{-E_{surf}\varepsilon_{eig} + \nu\sigma_{zz}}{1 - \nu} \quad (7)$$

σ_{zz} is the change in total vertical stress associated with a change in groundwater level Δh :

$$\sigma_{zz} = -\phi \rho g \Delta h \quad (8)$$

where ϕ is the porosity of the aquifer layers. Note that negative stresses correspond to compressive stresses in this work. Substituting Equations (3), (7) and (8) into (4) and integrating the vertical strain over an aquifer of thickness b and radius a yields the following vertical deformation field at the surface:

$$u_{z,exp}(r) = \begin{cases} \frac{(1 + \nu)(1 - 2\nu)}{(1 - \nu)} \frac{(\beta - \phi)\rho g \Delta h(r)b}{E_{surf}}, & r \leq a \\ 0, & r > a \end{cases} \quad (9)$$

Note that the poroelastic expansion described by Equation (9) accounts for changes in water weight ($\phi \rho g \Delta h$) associated with pore pressure fluctuations.

While we assume horizontal deformation to be negligible within the thickness of the aquifer layers, eigenstrains impose shear stresses at the base of the aquifer which results in both horizontal and vertical displacements. We can solve for this basal shear stress, $\sigma_{rz}(z = b)$, by considering the stress equilibrium equations for an axisymmetric problem in cylindrical coordinates (Wang, 2000):

$$\frac{\partial \sigma_{rz}}{\partial r} + \frac{\partial \sigma_{zz}}{\partial z} + \frac{\sigma_{rz}}{r} = 0 \quad (10)$$

340

$$\frac{\partial \sigma_{rz}}{\partial z} + \frac{\partial \sigma_{rr}}{\partial r} + \frac{\sigma_{rr} - \sigma_{\theta\theta}}{r} = 0 \quad (11)$$

 341 Substituting Equation (7) into (11) and integrating with respect to z yields:

$$\sigma_{rz}(z=b) - \sigma_{rz}(z=0) = -\int_0^b \frac{\partial}{\partial r} \left[\frac{-E_{surf}\varepsilon_{eig} + \nu\sigma_{zz}}{1-\nu} \right] \partial z \quad (12)$$

$$= \frac{\partial}{\partial r} I(r) \quad (13)$$

342 where

$$I(r) = \int_0^b \frac{E_{surf}\varepsilon_{eig} - \nu\sigma_{zz}}{1-\nu} \partial z \quad (14)$$

343 is the fundamental quantity driving poroelastic deformation (Fleitout & Chanard, 2018).

 344 Assuming that E_{surf} , ε_{eig} , ν and σ_{zz} are constant with depth and applying a zero shear
 345 stress boundary condition at the surface ($\sigma_{rz}(z=0)$), Equation (12) becomes:

$$\sigma_{rz}(z=b) = \frac{\partial}{\partial r} \left[\frac{(E_{surf}\varepsilon_{eig} - \nu\sigma_{zz})b}{1-\nu} \right] \quad (15)$$

$$= \frac{(\beta(1-2\nu) + \phi\nu)\rho g \Delta h b}{(1-\nu)} \frac{\partial}{\partial r} [\mathcal{H}(r-a) - 1] \quad (16)$$

$$= I\delta(r-a) \quad (17)$$

 346 where \mathcal{H} and δ are the Heaviside and Dirac delta functions, respectively. Finally, we pre-
 347 dict the deformation induced by $\sigma_{rz}(z=b)$ with the expressions derived by Johnson
 348 (1987) for surface displacements due to an axisymmetric shear stress distribution, $q(t)$:

$$u_{z, shear}(r) = \begin{cases} -\frac{(1-2\nu)(1+\nu)}{\pi E_{deep}} \int_r^a q(t) dt, & r \leq a \\ 0, & r > a \end{cases} \quad (18)$$

$$u_{r, shear}(r) = \frac{4(1-\nu^2)}{\pi E_{deep}} \int_0^a \frac{t}{t+r} q(t) \left[\left(\frac{2}{k^2} - 1 \right) \mathcal{K}(k) - \frac{2}{k^2} \mathcal{E}(k) \right] dt \quad (19)$$

 349 where $k^2 = 4tr/(t+r)^2$. Using $\sigma_{rz}(z=b)$ as $q(t)$, inclusive limits of integration and
 350 the sifting property of the Dirac delta function results in:

$$u_{z, shear}(r) = \begin{cases} -\frac{(1-2\nu)(1+\nu)}{\pi E_{deep}} I, & r \leq a \\ 0, & r > a \end{cases} \quad (20)$$

$$u_{r, shear}(r) = \frac{4(1-\nu^2)}{\pi E_{deep}} I \frac{a}{a+r} \left[\left(\frac{2}{k^2} - 1 \right) \mathcal{K}(k) - \frac{2}{k^2} \mathcal{E}(k) \right] \quad (21)$$

 351 where $k^2 = 4ar/(a+r)^2$. Since $\mathcal{K}(k)$ diverges when $r = a$, we express and evaluate
 352 the $\mathcal{K}(k)$ and $\mathcal{E}(k)$ terms with infinite series as:

$$\left(\frac{2}{k^2} - 1 \right) \mathcal{K}(k) - \frac{2}{k^2} \mathcal{E}(k) = \frac{\pi}{2} \sum_{n=0}^{\infty} \frac{n}{n+1} \left(\frac{(2n)!}{2^{2n}(n!)^2} \right)^2 k^{2n} \quad (22)$$

353 To obtain an order of magnitude estimate of the poroelastic displacements expected
 354 in OPAS, we compute the poroelastic deformation generated by a 40 m increase in ground-
 355 water level - the largest fluctuation observed in OPAS - in unconfined disk aquifers with
 356 radii of 100 km and 250 km and a thickness of 1000 m (Figure 7B). The vertical displace-
 357 ment is largely due to poroelastic expansion and is bounded by the aquifer. The hori-
 358 zontal poroelastic displacement, on the other hand, is entirely shear-induced and extend
 359 beyond the aquifer. Moreover, the amplitude of deformation is independent of the wave-
 360 length of pore pressure perturbation in contrast to the surface loading case. Indeed, the
 361 100 km and 250 km disks result in displacements of the same amplitude.

362 4.1.3 Arbitrary 2D poroelastic eigenstrains in an elastic half-space

363 When the 2D spatial distribution of quantity I (Equation (14)) is arbitrary - as is
364 the case for OPAS - we can first decompose $I(x, y)$ into its Fourier components as:

$$I(x, y) = \sum_{k_x, k_y} A_1(k_x, k_y) \cos(k_x x) \cos(k_y y) + A_2(k_x, k_y) \cos(k_x x) \sin(k_y y) \\ + A_3(k_x, k_y) \sin(k_x x) \cos(k_y y) + A_4(k_x, k_y) \sin(k_x x) \sin(k_y y) \quad (23)$$

365 where k_x and k_y are the wavenumbers in the x and y directions. Similar to Equation (21),
366 the horizontal displacement field can then be computed as:

$$u_x = \frac{2(1 - \nu^2)}{E_{deep}} \sum_{k_x, k_y} -A_1(k_x, k_y) \sin(k_x x) \cos(k_y y) - A_2(k_x, k_y) \sin(k_x x) \sin(k_y y) \\ + A_3(k_x, k_y) \cos(k_x x) \cos(k_y y) + A_4(k_x, k_y) \cos(k_x x) \sin(k_y y) \quad (24)$$

367

$$u_y = \frac{2(1 - \nu^2)}{E_{deep}} \sum_{k_x, k_y} -A_1(k_x, k_y) \cos(k_x x) \sin(k_y y) + A_2(k_x, k_y) \cos(k_x x) \cos(k_y y) \\ - A_3(k_x, k_y) \sin(k_x x) \sin(k_y y) + A_4(k_x, k_y) \sin(k_x x) \cos(k_y y) \quad (25)$$

368 4.2 Extraction of geodetic poroelastic displacements

369 In order to extract poroelastic deformation from GNSS time series, we first assume
370 that deformation from hydrological loading is well reproduced by the GRACE model and
371 hence focus on the GNSS - GRACE residual time series. This assumption is supported
372 by a comparison of the vertical time series in Figures 8 and S2. The geodetic deforma-
373 tion at station ZKC1 located outside OPAS and other aquifer systems (Figure 3A) is well
374 explained by the GRACE model and presents very little residual seasonal displacements
375 (Figure 8A). This is consistent with Chanard et al. (2018)'s finding that vertical displace-
376 ments observed by GNSS are generally well explained by a GRACE loading model at
377 a global scale because most stations are located at bedrock sites. At station MOWS at
378 the center of OPAS, on the other hand, the GNSS vertical displacements deviate from
379 that predicted from loading effects and the residuals show clear seasonal and multiannual
380 features (Figure 8B).

381 For the horizontal components, we also estimate and remove the common mode de-
382 formation from the GNSS-GRACE residual time series to isolate OPAS's poroelastic re-
383 sponse. We estimate the common mode by taking the average of the horizontal GNSS-
384 GRACE residual time series. This step is necessary as Figure S5 illustrates that neigh-
385 bouring aquifers can induce significant horizontal poroelastic deformation within the study
386 region. Although the horizontal displacements in OPAS caused by the synthetic poroe-
387 lastic loading in Figure S5D are affected by boundary effects and vary with distance from
388 the load, most stations do move in the same direction, similar to the displacements ex-
389 tracted through our methodology but without removing the common mode (Figure S5C).
390 Subtracting the common mode from GNSS-GRACE residual time series should thus ac-
391 count for the first order effects of neighbouring aquifers.

392 We posit that at least part of these seasonal and multiannual residuals can be at-
393 tributed to instantaneous poroelastic deformation and should therefore be proportional
394 to and in phase with groundwater fluctuations. Since we know the dominant temporal
395 functions that make up the groundwater fluctuations, we can test this hypothesis by pro-
396 jecting the residual geodetic time series onto these functions. However, unlike the related
397 Principal Component Analysis (PCA) technique, ICA yields independent components
398 which are not constrained to be orthogonal. Before proceeding with the projection, we
399 must thus orthogonalize vectors V_1^{GW} , V_2^{GW} and V_3^{GW} from Section 3.1 via the Gram-
400 Schmidt process to obtain an orthogonal basis, enabling us to sum the contribution of

each basis vector as follows:

$$P_j = \frac{R_j \cdot W_1}{\|W_1\|^2} W_1 + \frac{R_j \cdot W_2}{\|W_2\|^2} W_2 + \frac{R_j \cdot W_3}{\|W_3\|^2} W_3 \quad (26)$$

where P_j is the inferred poroelastic displacement for direction j (i.e., east, north or up), R_j is the GNSS-GRACE residual time series and W_1, W_2, W_3 are the orthogonalized versions of $V_1^{GW}, V_2^{GW}, V_3^{GW}$. Figure S6 reveals that the V_i^{GW} 's were not far from orthogonality to start with since W_2 and W_3 only differ marginally from V_2^{GW} and V_3^{GW} , respectively.

The resulting P_j 's are shown in yellow in Figure 8 and Figure S2. The recovered vertical poroelastic deformation is relatively small at station ZKC1 outside of aquifer systems and relatively large at station MOWS at the center of OPAS. However, both stations exhibit similar amplitudes of horizontal poroelastic deformation. This behavior is consistent with the analytical solutions developed in Section 4.1.

4.3 Vertical poroelastic displacements

Figure 9 illustrates the amplitudes of the poroelastic signals extracted with each groundwater temporal function W_i . Similar to the groundwater spatial distributions in Figure 4, the vertical poroelastic signal recovered with W_1 is mostly positive and is more extensive and of higher amplitude than the signals recovered with W_2 and W_3 . The poroelastic signals associated with W_2 and W_3 present both positive and negative values like the S_2U_2 and S_3U_3 distributions of groundwater.

Focusing on this regional signal, Figure 9A shows that many stations outside OPAS exhibit amplitudes comparable to those inside OPAS. We attribute these poroelastic displacements to the other major aquifer systems present in the region (Figure 2). Westernmost stations (e.g., ZKC1) where major aquifer structures are sparse or non-existent display some of the smallest amplitudes. However, it is difficult to know whether or not a GNSS station is sitting on top of an aquifer system since the map in Figures 2 and S3 only indicates the surface outcrops of these aquifer systems. The particularly large seasonal displacements at station OKMU (Figure S2C) at the southwestern edge of OPAS might be due to intensive groundwater pumping. Unfortunately there is no nearby groundwater monitoring well active during this time period to test this hypothesis. Finally, as Eq. (9) suggests, the range of vertical poroelastic amplitudes observed within OPAS - from about 2 to 14 mm - may reflect differences in poroelastic (β, ϕ, E_{surf}) properties, groundwater variations (Δh) or aquifer thickness (b). We discuss this further in Section 5.

4.4 Horizontal poroelastic displacements

As for horizontal displacements, Figure 9D-F suggests that all three temporal functions W_i 's are associated with spatially heterogeneous poroelastic deformation on the order of a few millimeters. According to Equation (21), poroelastic horizontal displacements are governed by deep elastic parameters as opposed to the surficial properties relevant for vertical poroelastic expansion. Elastic properties are believed to be more laterally homogeneous at depth than at the surface. Indeed, as discussed in Section 5.2, surficial layers are more prone to fracturing which can alter elastic moduli. We thus approximate E_{deep} with a constant value of 80 GPa and use Equations (24) and (25) for a spatially variable 2D distribution $I(x, y)$ to predict the horizontal poroelastic deformation induced by the observed groundwater fluctuations.

The colormaps in Figure 9D-F show the spatial distributions of $I(x, y)$ interpolated within OPAS for each groundwater IC as well as the resulting displacements at the GNSS sites (red arrows). Although the model predictions associated with W_1 match the observed displacements to first order at a handful of stations within OPAS, the observa-

448 tions are more heterogeneous than predicted (Figure 9D). For example, station MOBW
 449 undergoes a 7 mm displacement to the southwest whereas the model predicts a sub-millimetric
 450 eastward displacement (Figure S2D). The models for W_2 and W_3 , on the other hand, fail
 451 at matching the extracted displacements (Figure 9EF).

452 There are a number of potential reasons for these discrepancies. First and foremost,
 453 horizontal poroelastic displacements are highly sensitive to local variations in ground-
 454 water levels since they depend on the gradient of the groundwater field (e.g., Eq. 13) and
 455 do not attenuate with decreasingly small perturbation wavelengths. Hence, the spatial
 456 resolution of the piezometric network might be insufficient to accurately model the hor-
 457 izontal deformation. Some of the large horizontal displacements might also be due to hy-
 458 drogeologic phenomena not included in the present model. For example, Silverii et al.
 459 (2016) and Serpelloni et al. (2018) explain horizontal transient signals observed around
 460 karstic aquifers with the opening and closing of vertical tensile dislocations due to ground-
 461 water variations. One way to improve the model would be to refine the spatial resolu-
 462 tion of surface deformation measurements using InSAR.

463 Finally, our projection methodology might be capturing sources of seasonal and multi-
 464 annual signals not associated with groundwater. In particular, Fleitout & Chanard (2018)
 465 show that important horizontal thermoelastic displacements can result from sharp vari-
 466 ations in elastic properties. Heterogeneities in hydrological loading not captured by GRACE
 467 might also be responsible for some of the discrepancy. However, this would require rel-
 468 atively strong heterogeneities since, as demonstrated in Figure 7A and as opposed to poroe-
 469 lastic deformation, the amplitude of deformation associated with elastic loading decreases
 470 with decreasing load size.

471 5 Aquifer mechanical properties

472 5.1 Estimating surficial elastic parameters from vertical geodetic mea- 473 surements

474 As discussed in Section 4, vertical poroelastic displacement is primarily due to the
 475 expansion and contraction of surficial layers in response to groundwater fluctuations. As-
 476 suming that the system is unconfined to first order and that the ICs extracted in Sec-
 477 tion 3 indeed capture the groundwater variations responsible for the poroelastic defor-
 478 mation, we can estimate an effective surficial Young modulus E_{surf} directly below each
 479 GNSS station by rearranging Eq. (9) as:

$$E_{surf} = \frac{(1 + \nu)(1 - 2\nu)}{(1 - \nu)} \frac{(\beta - \phi)\rho g \Delta h b}{u_{z,exp}} \quad (27)$$

480 To this end, we compare the interpolated groundwater fluctuations from Section
 481 3 to the inferred vertical poroelastic deformation from Section 4. For each GNSS sta-
 482 tion where both datasets are available, we consider the slope and coefficient of determi-
 483 nation, R^2 , of the best-fit line through the displacement vs groundwater level space (Fig-
 484 ure S7). The slope represents the ratio of vertical displacement to groundwater varia-
 485 tion, $u_{z,exp}/\Delta h$, whose inverse enters Eq. (27) and R^2 quantifies the fit of the linear re-
 486 gression. The higher R^2 is, the more correlated the two datasets are and, hence, the more
 487 confident we are in the E_{surf} estimate. Figure 10A shows examples of vertical displace-
 488 ment and groundwater level time series with different R^2 values and Figure 10B illus-
 489 trates the spatial distribution of R^2 . We only retain stations with $R^2 > 0.35$ such as
 490 MOC3, ARBT and MOSD to estimate E_{surf} . Station ARHR illustrates a case where
 491 the time series are too incoherent to infer a meaningful value of E_{surf} .

492 For the thickness b , we assume that there is significant hydraulic connectivity be-
 493 tween the different aquifer units making up OPAS (as evidenced by the temporal cor-
 494 relation in Figure 6A) and sum their thicknesses. Figure 10C shows the total thickness

495 derived from Westerman et al. (2016)'s hydrogeological model. We extrapolate this thick-
 496 ness distribution for GNSS stations that are within 0.2° of the OPAS surface trace. Fi-
 497 nally, assuming representative constant values of $\beta = 0.80$ and $\phi = 0.25$ (Domenico
 498 & Schwartz, 1998), we can obtain an estimate of E_{surf} at the 30 retained sites where
 499 all three datasets ($\Delta h, b$ and $u_{z,exp}$) are available (Figure 10D). We also interpolate be-
 500 tween stations given that the vertical poroelastic field is governed by the relatively ho-
 501 mogeneous spatial distribution associated with W_1 (Figure 9A). The inset in Figure 10D
 502 reveals that the distribution of E_{surf} mostly falls between 1 and 10 GPa. We discuss these
 503 values further in Section 5.2.

504 Stations with low R^2 might reflect localities where spatial interpolation of the ground-
 505 water ICs fails to reproduce the actual variations in groundwater levels. For example,
 506 station ARHR and two of its neighbours which also display low R^2 values are all located
 507 in a region with relatively few piezometric measurements. Nevertheless, the fact that we
 508 obtain coherent ($R^2 > 0.35$) geodetic and groundwater time series and realistic values
 509 of E_{surf} at 30 out of the 41 eligible GNSS stations within OPAS, suggests that our method-
 510 ology is adequate for most sites.

511 5.2 Explaining low field estimates of E_{surf}

512 In Section 5.1 we estimated a spatial distribution for E_{surf} with values ranging from
 513 0.5 to 20 GPa. These values are lower than the laboratory-constrained elastic moduli
 514 of the principal rocks found in OPAS: limestone, dolomite, sandstone and shale (West-
 515 erman et al., 2016). For example, Ge & Garven (1992) suggest values of 125, 68, 9 and
 516 11 GPa for the Young modulus of Blair Dolomite, Maxville Limestone, Berea Sandstone
 517 and Chattanooga Shale, respectively (see Figure S8), pointing to an average Young mod-
 518 ulus of the order of 50 GPa.

519 There is a growing body of evidence that laboratory-based values overpredict *in*
 520 *situ* estimates of effective elastic moduli (e.g., Matonti et al., 2015; Bailly et al., 2019).
 521 Matonti et al. (2015), for instance, report seismic velocities, V_p , measured on carbonate
 522 rock outcrops that are up to 70% smaller than those obtained on rock samples in the lab-
 523 oratory, implying a tenfold reduction in elastic moduli. Although part of the discrepancy
 524 is probably due to the greater porosity observed in the field (e.g., due to karstic features
 525 in this case), Fortin et al. (2007) and Bailly et al. (2019) have shown that seismic veloc-
 526 ities - and hence elastic moduli - are more sensitive to geological features with high as-
 527 pect ratios such as cracks, fractures, bedding plane and faults because they are more com-
 528 pliant to deformation than spherical pores.

529 Following the effective medium theory framework of Fortin et al. (2007), the rati-
 530 o of effective bulk modulus K to bulk modulus of the intact rock, K_o , can be described
 531 in terms of porosity, ϕ , and fracture density, f , defined as $f = Nc^3/V$ where N is the
 532 number of fracture characterized by a radius c , embedded in a volume V (Walsh, 1965):

$$\frac{K_o}{K} = 1 + \frac{3}{2} \frac{(1 - \nu_o)}{(1 - 2\nu_o)} \phi + \frac{16}{9} \frac{(1 - \nu_o^2)}{(1 - 2\nu_o)} f \quad (28)$$

533 where ν_o is the Poisson ratio of the intact rock. Assuming $\nu_o = 0.25$, Eq. (28) reduces
 534 to:

$$\frac{K_o}{K} = 1 + 2.25\phi + 3.33f \quad (29)$$

535 Thus, a fourfold reduction in elastic modulus ($K_o/K = 4$) for example would re-
 536 quire - assuming a spherical pore porosity of 25% - a fracture density f of 0.7, a com-
 537 mon value reported in fractured reservoirs (Bailly et al., 2019). We thus conclude that
 538 the reduction in elastic moduli is mostly due to the presence of fracture-like geological
 539 features as in previous studies (Matonti et al., 2015; Bailly et al., 2019).

6 Discussion and Conclusions

To summarize, in this study, we characterized the spatiotemporal variations of OPAS's groundwater levels with three independent components. In particular, we uncovered a regional-scale groundwater signal that is temporally correlated with geodetic observations. Then, by assuming that hydrological loading displacements are well described by a GRACE-based model and that poroelastic deformation is in phase with groundwater fluctuations, we extracted vertical and horizontal poroelastic displacement fields from GNSS time series by projecting onto the groundwater components. We also quantified the amplitudes of displacements induced by hydrological vs poroelastic loading with analytical solutions and developed a 2D poroelastic model to relate groundwater perturbations in an unconfined aquifer system to surface displacements. Finally, we found that the extracted groundwater variations and vertical poroelastic displacements imply an heterogeneous spatial distribution of Young modulus ranging from 0.5 to 20 GPa.

Our findings have important implications in the fields of hydrology, geodesy and seismology. First, the excellent correlation between the GRACE and groundwater temporal functions indicates that there is consistency between the water mass fluctuations observed at the local and continental scales. Filtering groundwater levels dataset with ICA could also lead to improved piezometric maps free of aberrant local signals. In terms of poroelastic displacements, the OPAS example clearly demonstrates that both hydrological loading and poroelastic effects can induce significant geodetic deformation in the vertical and horizontal directions - hence the need to account for both deformation fields when correcting GNSS time series for hydrological effects. Since the two types of deformation can interfere destructively, failing to account for poroelastic effects in hydrogeodetic inversions could result in underestimation of total water storage variations. The notion that poroelastic stresses may be locally stronger than those generated from elastic loading (due to their relative amplitudes at small perturbation wavelengths) also warrants revisiting the role of both sources of stress in triggering seasonal seismicity (Craig et al., 2017). Lastly, our relatively low geodetic estimates of Young modulus motivates further investigation into surficial elastic parameters and their effect on global surface loading models (Chanard et al., 2018).

While this study is clarifying the signature of large aquifer systems in GNSS time series, further work is certainly necessary to address the current limitations of our methodology, starting with testing the validity of the method in other aquifer settings. In particular, the methodology should be evaluated in non-karstic and/or confined aquifer environments as well as in systems undergoing inelastic deformation. Furthermore, we recognize that the signals we attribute to poroelastic origins may be contaminated by other sources of seasonal signals, either due to deformation from thermal, atmospheric and residual hydrological loading effects or to systematic errors in the GRACE and GNSS data processing. Chanard et al. (2020) report draconitic signals, aliasing from mismodelled tides, tropospheric delays and other environmental effects as potential sources of seasonal noise and systematic errors in GNSS datasets. Perhaps most importantly, our work suggests that horizontal poroelastic displacements are highly sensitive to spatial variations in groundwater, making it difficult to accurately extract them from GNSS time series without a sufficient resolution of the piezometric surface. Future work will thus focus on characterizing the horizontal deformation field that would help identify possible local effects in the vicinity of groundwater monitoring wells using InSAR displacement time series. In particular, a more complete characterization of surface horizontal displacements at the surface should lead to an improved understanding of how water is stored in the different aquifers units of the Ozark system (confined-unconfined) as well as their connections.

590

591

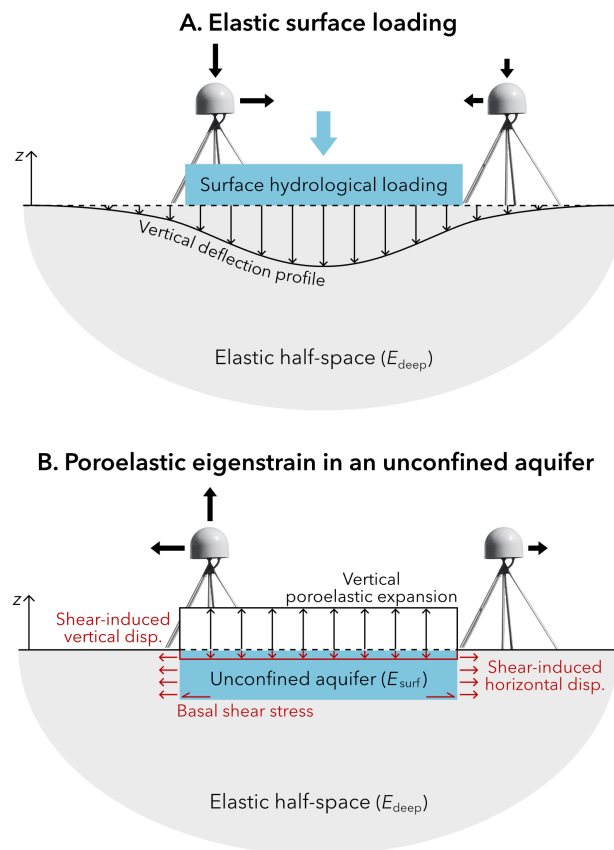


Figure 1. Deformation due to surface hydrological loading vs poroelastic eigenstrain. **A.** The addition of water mass causes ground subsidence and horizontal motion towards the added load. The surface vertical displacement expected from a circular load on an elastic half-space is shown. **B.** An increase in pore pressure in an aquifer leads to upward vertical and outward horizontal displacements. While most of the vertical deformation comes from poroelastic expansion, surface horizontal and vertical displacements also result from basal shear stresses.

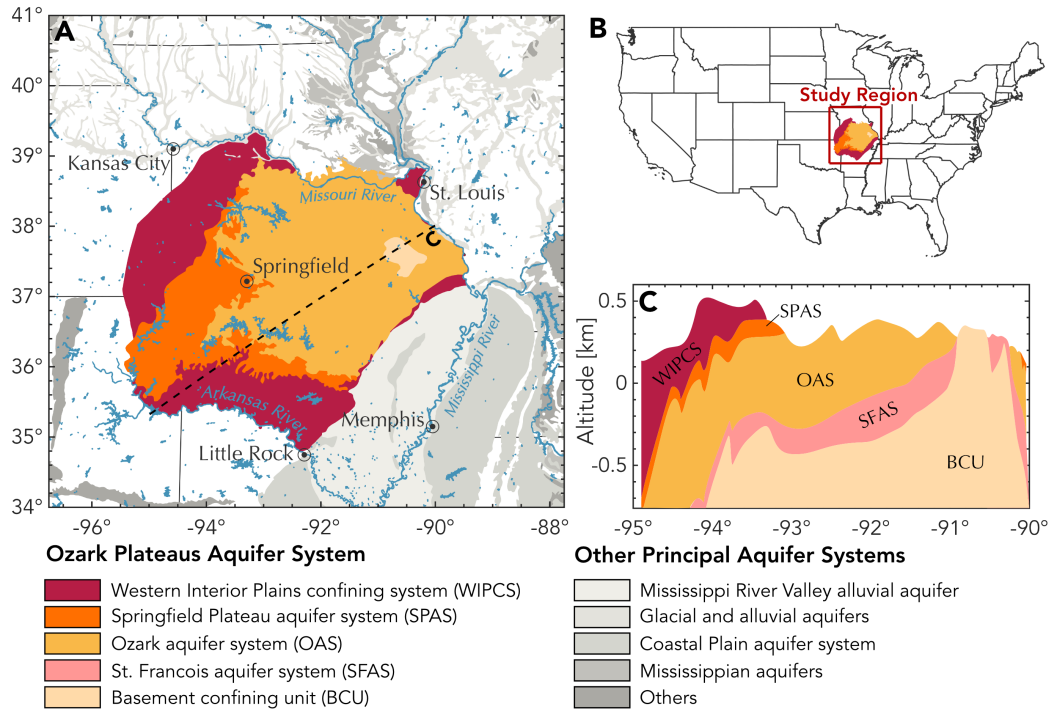


Figure 2. Regional hydrogeological setting. **A.** Simplified outcrop map of the Ozark Plateaus Aquifer System (OPAS) based on physiographic sections (modified from Hays et al. (2016) and Knierim et al. (2017)) and neighbouring aquifer systems (from USGS map of Principal Aquifers). **B.** Geographical location of OPAS. **C.** Hydrogeological cross-section at the dashed line in A based on Westerman et al. (2016).

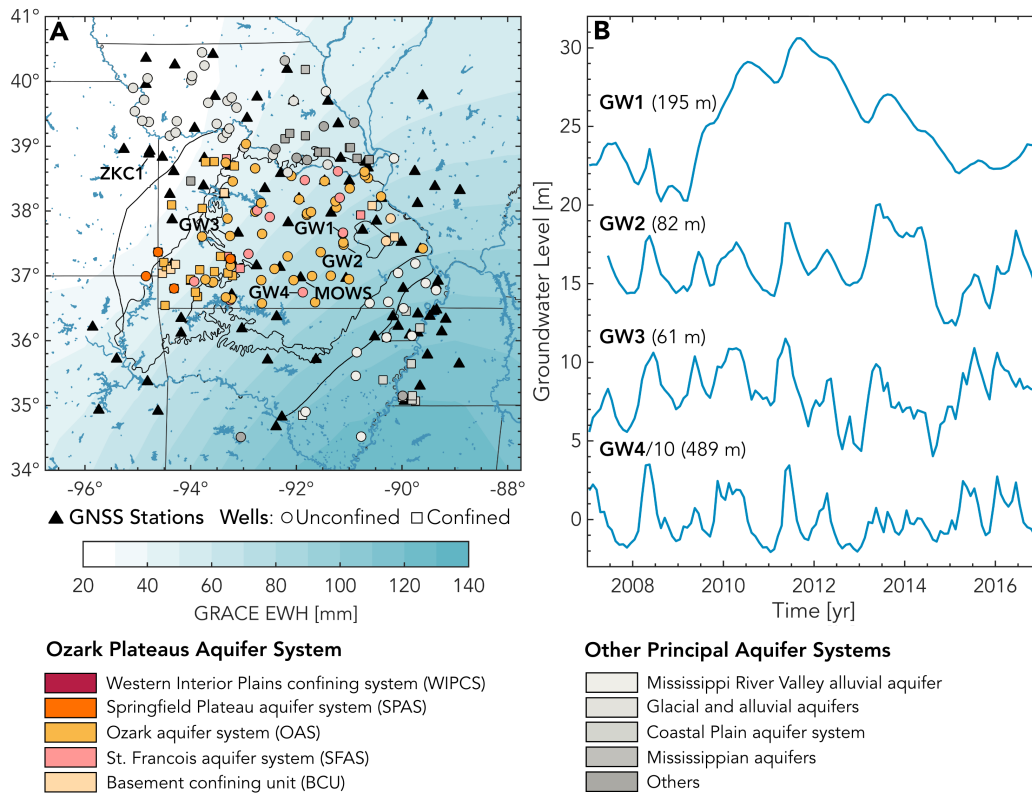


Figure 3. GNSS, GRACE and groundwater data sets. **A.** Annual EWH peak-to-peak amplitudes derived from GRACE and locations of GNSS stations and groundwater monitoring wells used in this study. The color of the well markers indicates the aquifer system at the base of a well and the shape describes the type of aquifer(s) - i.e., confined or unconfined - encountered by a well (as classified by the USGS). **B.** Example of groundwater time series at different locations across OPAS. Note that time series GW4 was divided by a factor of 10. Well depths are indicated in parenthesis. The featured wells correspond to USGS site numbers 373955091065901 (GW1), 372853091061801 (GW2), 373701093151601 (GW3) and 364324091515001 (GW4).

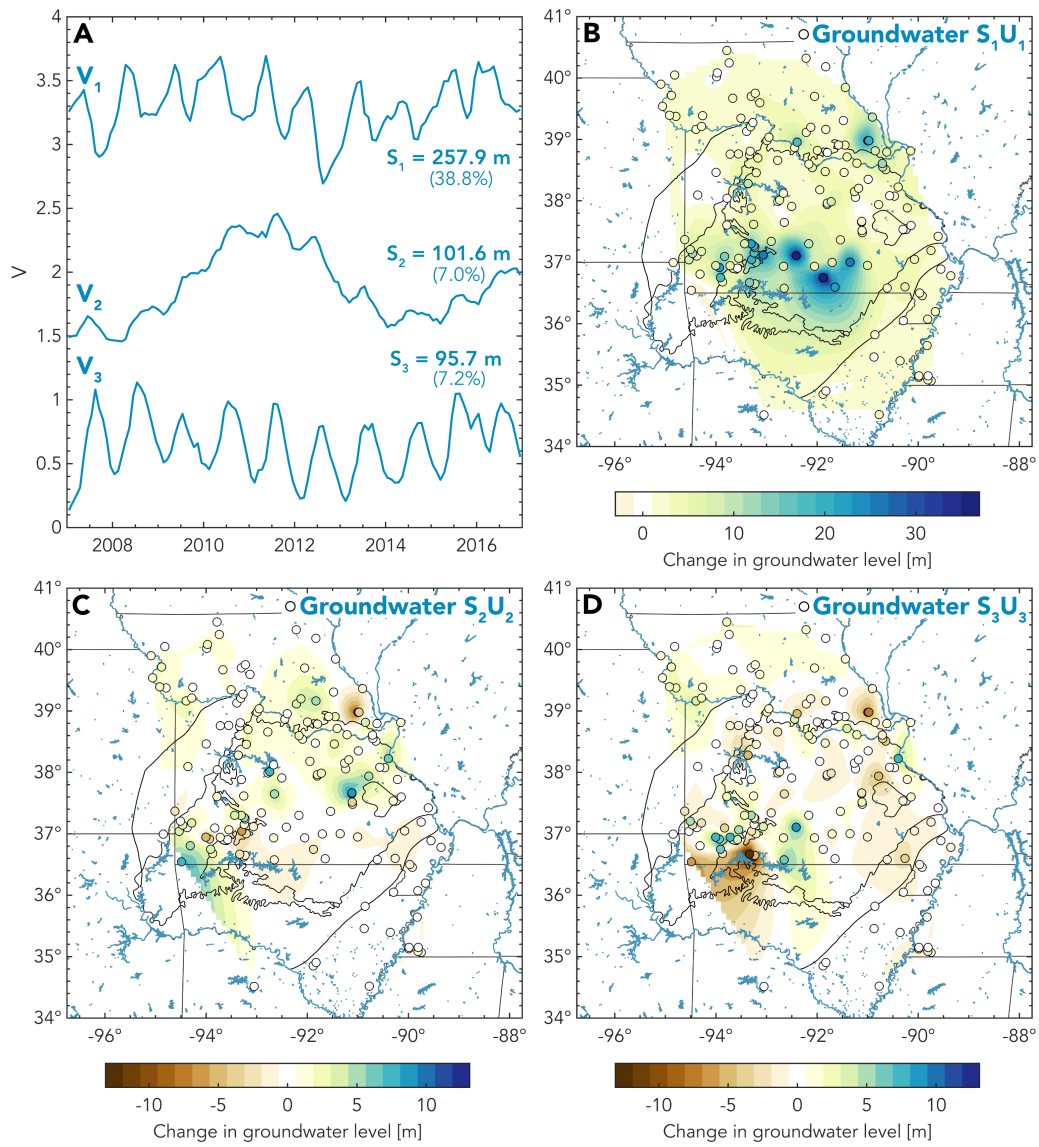


Figure 4. ICA decomposition of the groundwater dataset. A. Temporal evolution and weighting factors of the three components ICA. The variance of the groundwater dataset explained by each component is also indicated in parenthesis. **B-D** Weighted spatial distributions of the three components (circles). Spatial interpolation of the distributions is also shown.

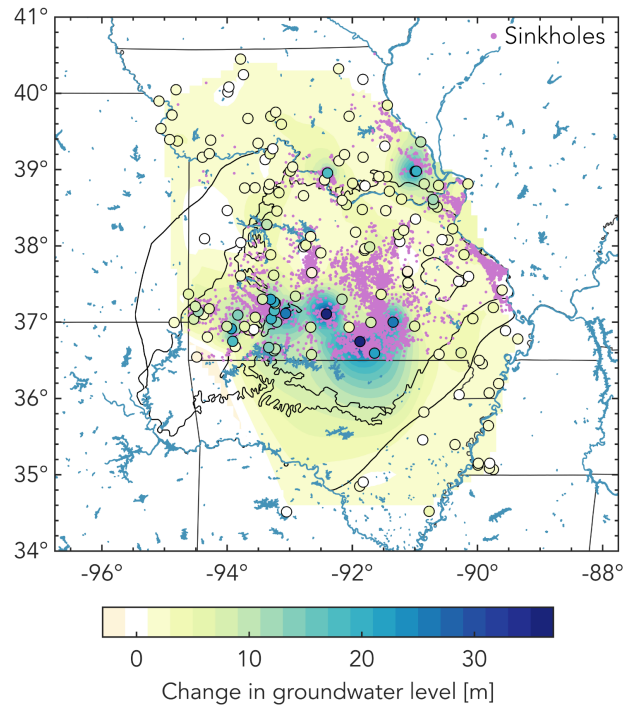


Figure 5. Spatial correlation between sinkholes (proxy for karstification) and groundwater IC1. Purple dots indicate the location of known sinkholes in Missouri as reported by the Missouri Geological Survey (<https://dnr.mo.gov/geology/geosrv/envgeo/sinkholes.htm>). The spatial distribution of IC1 groundwater (same as Figure 4B) is shown for comparison.

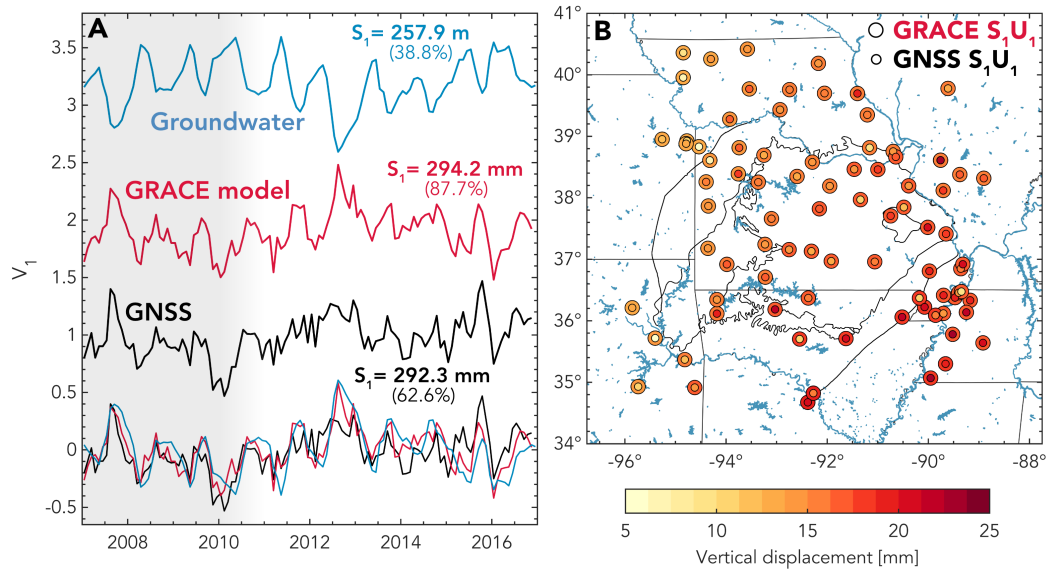


Figure 6. Temporal correlation between the first independent component of groundwater and the GRACE-predicted and GNSS vertical displacements. A. Temporal evolution and weighting factor (and variance explained) for each dataset. The 3 temporal functions are replotted at the bottom of the figure (note that the groundwater function is flipped) to facilitate visual comparison. The grey shaded area indicates the timespan prior to the installation of most GNSS stations sitting on top of OPAS from 2010 to 2011. **B.** Spatial distribution of the GRACE-predicted (outer circles) and GNSS (inner circles) vertical displacement datasets.

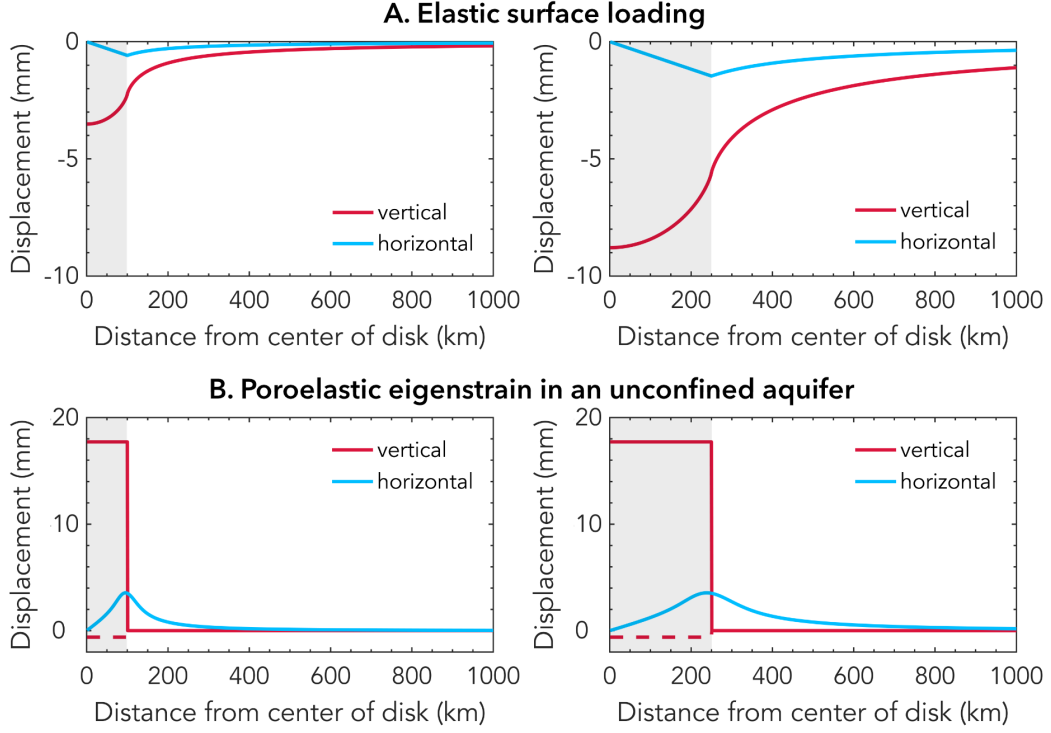


Figure 7. Surface displacements due to elastic loading vs poroelastic eigenstrain. Vertical and horizontal surface displacements induced by (A) a disk load at the surface of an elastic half-space and (B) poroelastic eigenstrain in a circular unconfined aquifer as illustrated in Figure 1 for disks of radius $a = 100$ km (left) and $a = 250$ km (right) as indicated by the grey-shaded areas. For the vertical poroelastic deformation, the dashed line represents the shear-induced deformation while the solid line represents the total poroelastic displacement. We use the maximum EWH (150 mm) and groundwater level (40 m) fluctuations observed in OPAS for P and Δh , respectively. Other parameter values are: $\nu = 0.25$, $E_{deep} = 80$ GPa, $E_{surf} = 10$ GPa, $\beta = 0.8$, $\phi = 0.25$, $b = 1000$ m.

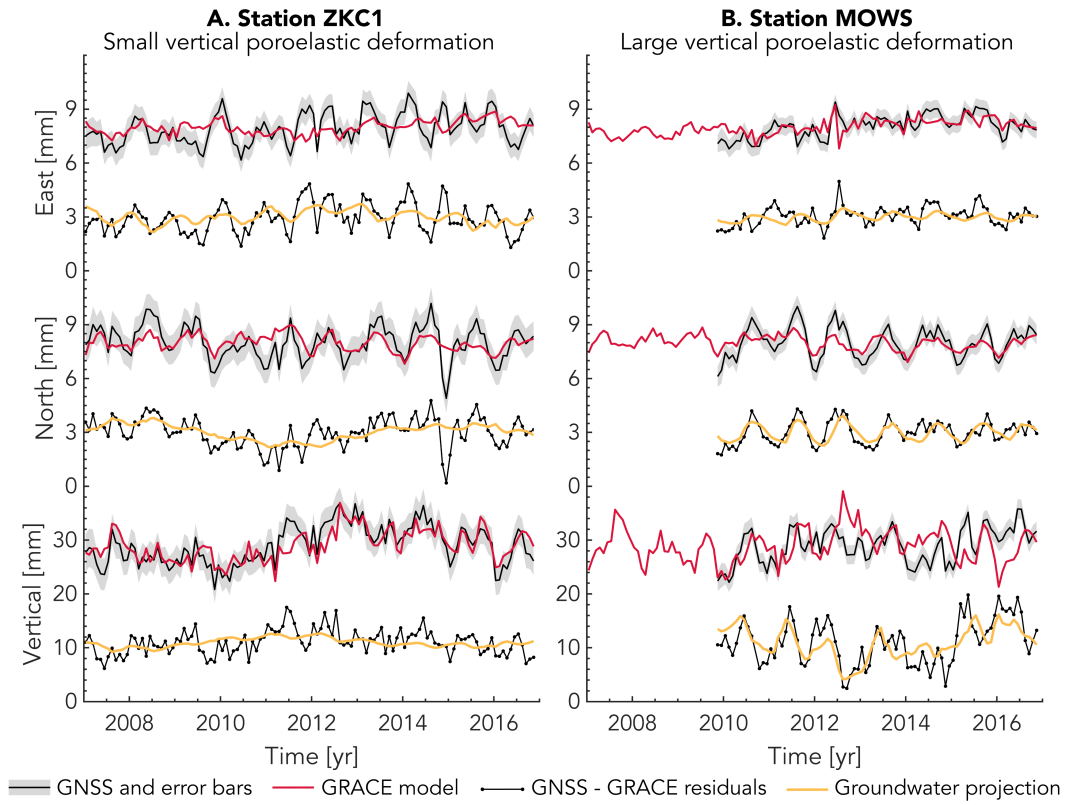


Figure 8. Extracting the OPAS's poroelastic signal from GNSS time series. Black lines with grey error bars are GNSS time series (corrected for degree 1). A common mode has been removed in the East and North components. Red lines are the GRACE predictions. Black dots are the GNSS-GRACE residuals. Yellow lines are the projection of the GNSS-GRACE residuals onto the W_i from the groundwater ICA.

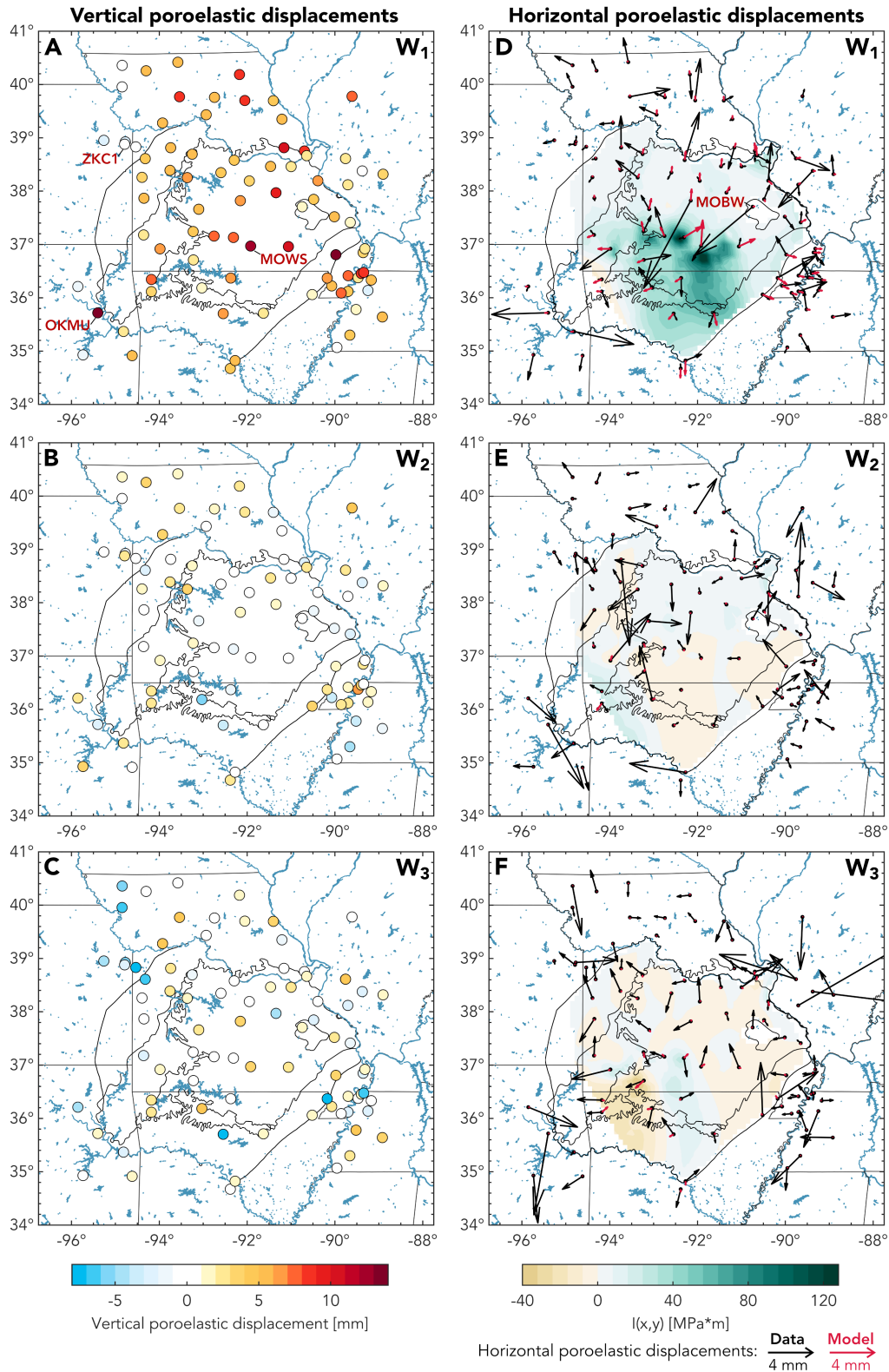


Figure 9. Inferred poroelastic displacements and poroelastic model predictions Vertical (A-C) and horizontal (D-F) poroelastic displacement extracted by projecting onto the different temporal functions W_i . **D-F.** Distribution of $I(x,y)$ from each groundwater IC and resulting horizontal poroelastic displacement (red arrows).

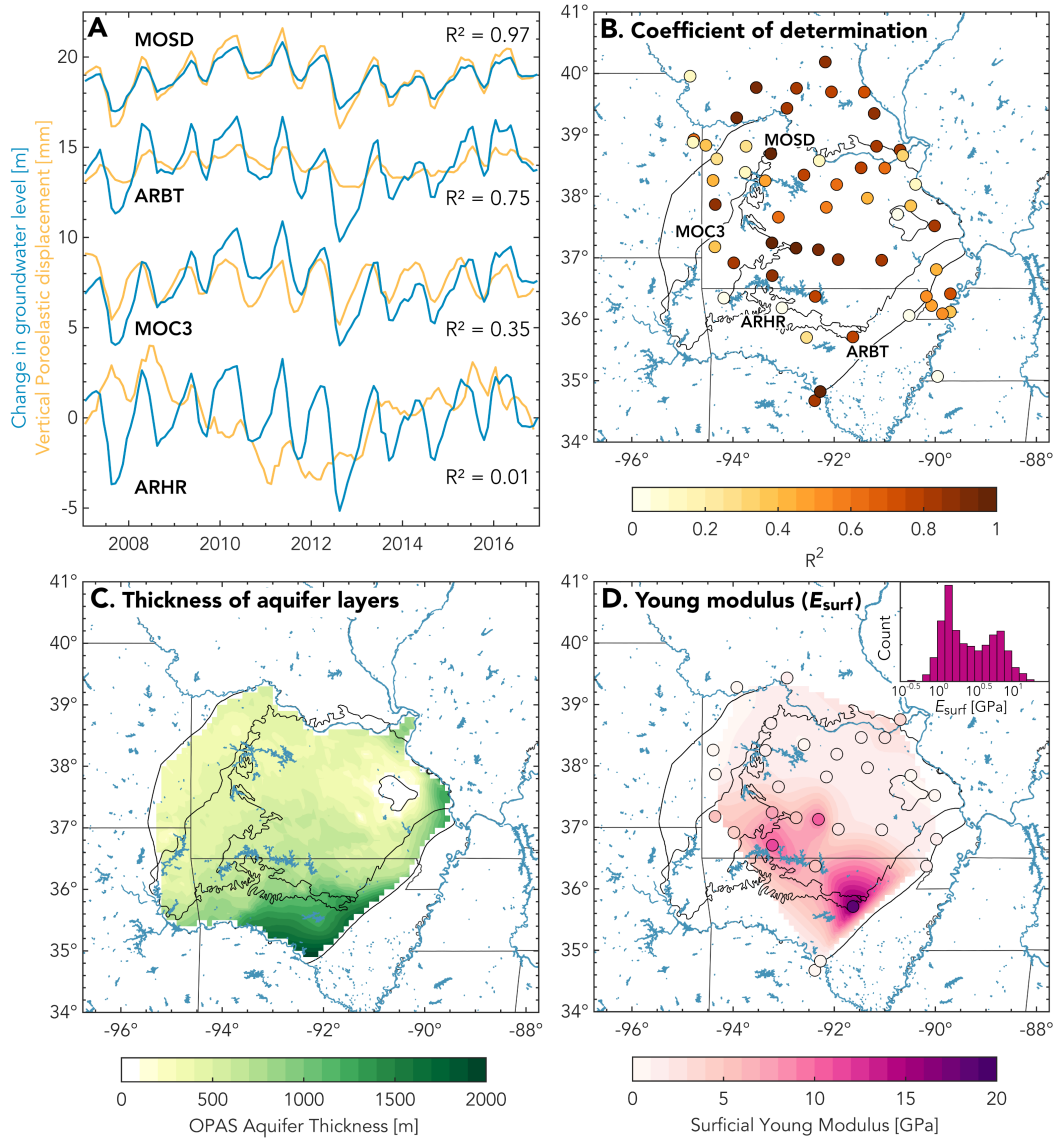


Figure 10. Estimating surficial Young modulus from vertical poroelastic displacement and groundwater level variations **A.** Examples of vertical poroelastic displacement time series and groundwater level change extracted with ICA and interpolated at the GNSS stations location. **B.** Coefficient of determination (R^2) of a linear fit through poroelastic displacement vs change in groundwater level. The higher R^2 , the better the E_{surf} estimate. **C.** Total thickness of the aquifer layers. **D.** Young's Modulus computed for $R^2 > 0.35$ and where all three input variables are available. Inset: Distribution of Young's modulus

592

593 Acknowledgments

594 The USGS groundwater level, CSR GRACE and NGL GNSS time series used in this work
 595 are available at <https://waterservices.usgs.gov>, https://podaac.jpl.nasa.gov/dataset/GRACE_GSM_L2_GRAV_CSR_RL06 and <http://geodesy.unr.edu>, respectively. The
 596 Ozark Plateaus Aquifer System model of Westerman et al. (2016) is available at <http://dx.doi.org/10.5066/F7HQ3X0T>.
 597
 598

599 References

- 600 Adusumilli, S., Borsa, A. A., Fish, M. A., McMillan, H. K., & Silverii, F. (2019).
 601 A Decade of Water Storage Changes Across the Contiguous United States From
 602 GPS and satellite gravity. *Geophysical Research Letters*, 2019GL085370. doi:
 603 10.1029/2019GL085370
- 604 Alghamdi, A., Hesse, M. A., Chen, J., & Ghattas, O. (2020). Bayesian Poroelastic
 605 Aquifer Characterization From InSAR Surface Deformation Data. Part I: Maxi-
 606 mum A Posteriori Estimate. *Water Resources Research*, 56(10), e2020WR027391.
 607 Retrieved from <https://onlinelibrary.wiley.com/doi/10.1029/2020WR027391>
 608 doi: 10.1029/2020WR027391
- 609 Altamimi, Z., Rebischung, P., Métivier, L., & Collilieux, X. (2016). ITRF2014: A
 610 new release of the International Terrestrial Reference Frame modeling nonlinear
 611 station motions. *Journal of Geophysical Research: Solid Earth*, 121(8), 6109–6131.
 612 doi: 10.1002/2016JB013098
- 613 Amelung, F., Galloway, D. L., Bell, J. W., Zebker, H. A., & Laczniak, R. J. (1999,
 614 6). Sensing the ups and downs of las vegas: Insar reveals structural control of land
 615 subsidence and aquifer-system deformation. *Geology*, 27, 483. doi: 10.1130/0091-
 616 -7613(1999)027<0483:STUADO>2.3.CO;2
- 617 Argus, D. F., Fu, Y., & Landerer, F. W. (2014). Seasonal variation in total water
 618 storage in California inferred from GPS observations of vertical land motion. *Geo-
 619 physical Research Letters*, 41(6), 1971–1980. doi: 10.1002/2014GL059570
- 620 Argus, D. F., Landerer, F. W., Wiese, D. N., Martens, H. R., Fu, Y., Famiglietti,
 621 J. S., . . . Watkins, M. M. (2017, dec). Sustained Water Loss in California’s
 622 Mountain Ranges During Severe Drought From 2012 to 2015 Inferred From
 623 GPS. *Journal of Geophysical Research: Solid Earth*, 122(12), 10,559–10,585.
 624 doi: 10.1002/2017JB014424
- 625 Bailly, C., Fortin, J., Adelinet, M., & Hamon, Y. (2019, dec). Upscaling of Elastic
 626 Properties in Carbonates: A Modeling Approach Based on a Multiscale Geophys-
 627 ical Data Set. *Journal of Geophysical Research: Solid Earth*, 124(12), 13021–
 628 13038. doi: 10.1029/2019JB018391
- 629 Bayless, E. R., Arihood, L. D., Reeves, H. W., Sperl, B. J., Qi, S. L., Stipe, V. E.,
 630 & Bunch, A. R. (2017). *Maps and grids of hydrogeologic information created
 631 from standardized water-well drillers’ records of the glaciated United States* (Tech.
 632 Rep.). doi: 10.3133/sir20155105
- 633 Bell, J. W., Amelung, F., Ferretti, A., Bianchi, M., & Novali, F. (2008, 2). Per-
 634 manent scatterer insar reveals seasonal and long-term aquifer-system response to
 635 groundwater pumping and artificial recharge. *Water Resources Research*, 44. doi:
 636 10.1029/2007WR006152
- 637 Bettadpur, S. (2018). Gravity Recovery and Climate Experiment Level-2 Gravity
 638 Field Product User Handbook. , 734, 1–21.
- 639 Bettinelli, P., Avouac, J.-P., Flouzat, M., Bollinger, L., Ramillien, G., Rajaure, S.,
 640 & Sapkota, S. (2008). Seasonal variations of seismicity and geodetic strain in the
 641 Himalaya induced by surface hydrology. *Earth and Planetary Science Letters*,
 642 266(3-4), 332–344. doi: 10.1016/J.EPSL.2007.11.021

- 643 Bevis, M., & Brown, A. (2014). Trajectory models and reference frames for crustal
644 motion geodesy. *Journal of Geodesy*, *88*(3), 283–311. doi: 10.1007/s00190-013-
645 -0685-5
- 646 Blewitt, G., Hammond, W. C., & Kreemer, C. (2018). Harnessing the GPS data ex-
647 plosion for interdisciplinary science. *Eos*, *99*. doi: 10.1029/2018EO104623
- 648 Blewitt, G., Lavallée, D., Clarke, P., & Nurutdinov, K. (2001). A new global
649 mode of Earth deformation: seasonal cycle detected. *Science (New York, N.Y.)*,
650 *294*(5550), 2342–5. doi: 10.1126/science.1065328
- 651 Borsa, A. A., Agnew, D. C., & Cayan, D. R. (2014, sep). Ongoing drought-induced
652 uplift in the western United States. *Science*, *345*(6204), 1587–1590. doi: 10.1126/
653 SCIENCE.1260279
- 654 Boussinesq, J. (1885). *Application des potentiels à l'étude de l'équilibre et du mouve-*
655 *ment des solides élastiques*. Blanchard: Reprint Paris.
- 656 Calais, E., Camelbeeck, T., Stein, S., Liu, M., & Craig, T. J. (2016). A new
657 paradigm for large earthquakes in stable continental plate interiors. *Geophys-*
658 *ical Research Letters*, *43*(20), 10,621–10,637. doi: 10.1002/2016GL070815
- 659 Carlson, G., Shirzaei, M., Ojha, C., & Werth, S. (2020, 9). Subsidence-derived
660 volumetric strain models for mapping extensional fissures and constraining rock
661 mechanical properties in the san joaquin valley, california. *Journal of Geophysical*
662 *Research: Solid Earth*, *125*. Retrieved from [https://onlinelibrary.wiley.com/](https://onlinelibrary.wiley.com/doi/10.1029/2020JB019980)
663 [doi/10.1029/2020JB019980](https://onlinelibrary.wiley.com/doi/10.1029/2020JB019980) doi: 10.1029/2020JB019980
- 664 Chanard, K., Fleitout, L., Calais, E., Rebischung, P., & Avouac, J. (2018). To-
665 ward a Global Horizontal and Vertical Elastic Load Deformation Model Derived
666 from GRACE and GNSS Station Position Time Series. *Journal of Geophysical*
667 *Research: Solid Earth*, *123*(4), 3225–3237. doi: 10.1002/2017JB015245
- 668 Chanard, K., Métois, M., Rebischung, P., & Avouac, J.-P. (2020). A warning against
669 over-interpretation of seasonal signals measured by the Global Navigation Satellite
670 System. *Nature Communications*, *11*(1), 1375. doi: 10.1038/s41467-020-15100-7
- 671 Chaussard, E., Bürgmann, R., Shirzaei, M., Fielding, E. J., & Baker, B. (2014). Pre-
672 dictability of hydraulic head changes and characterization of aquifer-system and
673 fault properties from InSAR-derived ground deformation. *Journal of Geophysical*
674 *Research: Solid Earth*, *119*(8), 6572–6590. doi: 10.1002/2014JB011266
- 675 Chaussard, E., Milillo, P., Bürgmann, R., Perissin, D., Fielding, E. J., & Baker, B.
676 (2017). Remote Sensing of Ground Deformation for Monitoring Groundwater
677 Management Practices: Application to the Santa Clara Valley During the 2012-
678 2015 California Drought. *Journal of Geophysical Research: Solid Earth*, *122*(10),
679 8566–8582. doi: 10.1002/2017JB014676
- 680 Choudrey, R. (2002). Variational methods for Bayesian independent component
681 analysis. *Robots.Ox.Ac.Uk*, 261. Retrieved from [http://www.robots.ox.ac.uk/](http://www.robots.ox.ac.uk/~parg/projects/ica/riz/Pubs/thesis.ps.gz)
682 [{~}parg/projects/ica/riz/Pubs/thesis.ps.gz](http://www.robots.ox.ac.uk/~parg/projects/ica/riz/Pubs/thesis.ps.gz)
- 683 Craig, T. J., & Calais, E. (2014). Strain accumulation in the new madrid and
684 wabash valley seismic zones from 14 years of continuous gps observation. *Journal*
685 *of Geophysical Research: Solid Earth*, *119*(12), 9110–9129.
- 686 Craig, T. J., Chanard, K., & Calais, E. (2017). Hydrologically-driven crustal stresses
687 and seismicity in the New Madrid Seismic Zone. *Nature Communications*, *8*(1),
688 2143. doi: 10.1038/s41467-017-01696-w
- 689 Domenico, P. A. P. A., & Schwartz, F. W. F. W. (1998). *Physical and chemical hy-*
690 *drogeology*. Wiley.
- 691 Dong, D., Fang, P., Bock, Y., Cheng, M. K., & Miyazaki, S. (2002). Anatomy of
692 apparent seasonal variations from GPS-derived site position time series. *Journal of*
693 *Geophysical Research: Solid Earth*, *107*(B4), ETG 9–1–ETG 9–16. doi: 10.1029/
694 2001JB000573
- 695 Farrell, W. E. (1972). Deformation of the Earth by surface loads. *Reviews of Geo-*
696 *physics*, *10*(3), 761. doi: 10.1029/RG010i003p00761

- 697 Ferreira, V., Ndehedehe, C., Montecino, H., Yong, B., Yuan, P., Abdalla, A., &
698 Mohammed, A. (2019). Prospects for Imaging Terrestrial Water Storage in
699 South America Using Daily GPS Observations. *Remote Sensing*, 11(6), 679. doi:
700 10.3390/rs11060679
- 701 Fleitout, L., & Chanard, K. (2018, December). Displacements and Stresses Induced
702 by Temperature and Poroelastic Pressure Variations in the Surficial layers for an
703 Earth with Realistic Elastic Properties. In *Agu fall meeting abstracts* (Vol. 2018,
704 p. G53B-03).
- 705 Fortin, J., Guéguen, Y., & Schubnel, A. (2007, aug). Effects of pore collapse and
706 grain crushing on ultrasonic velocities and V_p/V_s . *Journal of Geophysical Re-*
707 *search: Solid Earth*, 112(8). doi: 10.1029/2005JB004005
- 708 Fu, Y., Argus, D. F., & Landerer, F. W. (2015). GPS as an independent mea-
709 surement to estimate terrestrial water storage variations in Washington and
710 Oregon. *Journal of Geophysical Research: Solid Earth*, 120(1), 552–566. doi:
711 10.1002/2014JB011415
- 712 Galloway, D. L., & Burbey, T. J. (2011). Review: Regional land subsidence accom-
713 panying groundwater extraction. *Hydrogeology Journal*, 19(8), 1459–1486. doi: 10
714 .1007/s10040-011-0775-5
- 715 Ge, S., & Garven, G. (1992). Hydromechanical modeling of tectonically driven
716 groundwater flow with application to the Arkoma Foreland Basin. *Journal of Geo-*
717 *physical Research*, 97(B6), 9119. doi: 10.1029/92JB00677
- 718 Gleeson, T., Wagener, T., Döll, P., Zipper, S. C., West, C., Wada, Y., ... Bierkens,
719 M. F. P. (2021). Gmd perspective: the quest to improve the evaluation of
720 groundwater representation in continental to global scale models. *Geoscientific*
721 *Model Development Discussions*, 2021, 1–59. Retrieved from [https://](https://gmd.copernicus.org/preprints/gmd-2021-97/)
722 gmd.copernicus.org/preprints/gmd-2021-97/ doi: 10.5194/gmd-2021-97
- 723 GRACE. (2018). GRACE FIELD GEOPOTENTIAL COEFFICIENTS CSR RE-
724 LEASE 6.0 Ver. 6.0 PO.DAAC, CA, USA.
725 doi: 10.5067/GRGSM-20C06
- 726 Gualandi, A., & Liu, Z. (2021). Variational bayesian independent component
727 analysis for insar displacement time-series with application to central california,
728 usa. *Journal of Geophysical Research: Solid Earth*, 126, e2020JB020845. doi:
729 10.1029/2020JB020845
- 730 Gualandi, A., Serpelloni, E., & Belardinelli, M. E. (2016). Blind source separation
731 problem in GPS time series. *Journal of Geodesy*, 90(4), 323–341. doi: 10.1007/
732 s00190-015-0875-4
- 733 Hart, R. M., Clark, B. R., & Bolyard, S. E. (2008). *Digital Surfaces and Thick-*
734 *nesses of Selected Hydrogeologic Units within the Mississippi Embayment Regional*
735 *Aquifer Study (MERAS)* (Tech. Rep.).
- 736 Hays, P. D., Knierim, K. J., Breaker, B., Westerman, D. A., & Clark, B. R. (2016).
737 Hydrogeology and hydrologic conditions of the Ozark Plateaus aquifer system.
738 *U.S. Geological Survey Scientific Investigations Report*(2016-5137), 61.
- 739 Hu, X., & Bürgmann, R. (2020). Aquifer deformation and active faulting in Salt
740 Lake Valley, Utah, USA. *Earth and Planetary Science Letters*, 547, 116471. doi:
741 10.1016/J.EPSL.2020.116471
- 742 Imes, J. L. (1989). Analysis of the effect of pumping on groundwater flow in the
743 Springfield Plateau and Ozark Aquifers near Springfield, Missouri. *Water Re-*
744 *sources Investigations Report*, 89-4079.
- 745 Imes, J. L., & Emmett, L. F. (1994). Geohydrology of the Ozark Plateaus aquifer
746 system in parts of Missouri, Arkansas, Oklahoma, and Kansas. *US Geological Sur-*
747 *vey Professional Paper*, 1414 D. doi: 10.3133/pp1414d
- 748 Johnson. (1987). *Contact mechanics*. Cambridge University Press.
- 749 Johnson, C. W., Fu, Y., & Bürgmann, R. (2017). Seasonal water storage, stress
750 modulation, and California seismicity. *Science (New York, N.Y.)*, 356(6343),

- 1161–1164. doi: 10.1126/science.aak9547
- 751 King, N. E., Argus, D., Langbein, J., Agnew, D. C., Bawden, G., Dollar, R. S., . . .
 752 Barseghian, D. (2007). Space geodetic observation of expansion of the San Gabriel
 753 Valley, California, aquifer system, during heavy rainfall in winter 2004–2005. *Journal of Geophysical Research*, *112*(B3), B03409. doi: 10.1029/2006JB004448
 754
 755 Knierim, K. J., Nottmeier, A. M., Worland, S., Westerman, D. A., & Clark, B. R.
 756 (2017). Challenges for creating a site-specific groundwater-use record for the
 757 Ozark Plateaus aquifer system (central USA) from 1900 to 2010. *Hydrogeology*
 758 *Journal*. doi: 10.1007/s10040-017-1593-1
 759
 760 Kusche, J., Schmidt, R., Petrovic, S., & Rietbroek, R. (2009). Decorrelated grace
 761 time-variable gravity solutions by gfz, and their validation using a hydrological
 762 model. *Journal of geodesy*, *83*(10), 903–913.
 763
 764 Larochele, S., Gualandi, A., Chanard, K., & Avouac, J. P. (2018). Identifica-
 765 tion and Extraction of Seasonal Geodetic Signals Due to Surface Load Varia-
 766 tions. *Journal of Geophysical Research: Solid Earth*, *123*(12), 11,031–11,047. doi:
 10.1029/2018JB016607
 767
 768 Li, W., van Dam, T., Li, Z., & Shen, Y. (2016). Annual variation detected by gps,
 grace and loading models. *Studia Geophysica et Geodaetica*, *60*(4), 608–621.
 769
 770 Longuevergne, L., Florsch, N., & Elsass, P. (2007, 4). Extracting coherent regional
 771 information from local measurements with karhunen-loève transform: Case study
 772 of an alluvial aquifer (rhine valley, france and germany). *Water Resources Re-*
 773 *search*, *43*. Retrieved from <http://doi.wiley.com/10.1029/2006WR005000> doi:
 10.1029/2006WR005000
 774
 775 MATLAB. (2017). *9.3.0.713579 (r2017b)*. Natick, Massachusetts: The MathWorks
 Inc.
 776
 777 Matonti, C., Guglielmi, Y., Viseur, S., Bruna, P., Borgomano, J., Dahl, C., & Marié,
 L. (2015, jan). Heterogeneities and diagenetic control on the spatial distribution
 778 of carbonate rocks acoustic properties at the outcrop scale. *Tectonophysics*, *638*,
 779 94–111. Retrieved from [https://www.sciencedirect.com/science/article/](https://www.sciencedirect.com/science/article/pii/S0040195114005666)
 780 [pii/S0040195114005666](https://www.sciencedirect.com/science/article/pii/S0040195114005666) doi: 10.1016/J.TECTO.2014.10.020
 781
 782 Michel, S., Gualandi, A., & Avouac, J.-P. (2019). Interseismic coupling and slow slip
 events on the cascadia megathrust. *Pure and Applied Geophysics*, *176*(9), 3867–
 783 3891.
 784
 785 Miller, M. M., Shirzaei, M., & Argus, D. (2017). Aquifer Mechanical Properties and
 Decelerated Compaction in Tucson, Arizona. *Journal of Geophysical Research:*
 786 *Solid Earth*, *122*(10), 8402–8416. doi: 10.1002/2017JB014531
 787
 788 Mura, T. (1982). *General theory of eigenstrains*. Springer Netherlands. doi: 10.1007/
 978-94-011-9306-1_1
 789
 790 Ojha, C., Shirzaei, M., Werth, S., Argus, D. F., & Farr, T. G. (2018). Sus-
 791 tained Groundwater Loss in California’s Central Valley Exacerbated by In-
 792 tense Drought Periods. *Water Resources Research*, *54*(7), 4449–4460. doi:
 10.1029/2017WR022250
 793
 794 Ouellette, K. J., de Linage, C., & Famiglietti, J. S. (2013). Estimating snow wa-
 795 ter equivalent from GPS vertical site-position observations in the western United
 States. *Water Resources Research*, *49*(5), 2508–2518. doi: 10.1002/wrcr.20173
 796
 797 Riel, B., Simons, M., Ponti, D., Agram, P., & Jolivet, R. (2018). Quantifying
 798 Ground Deformation in the Los Angeles and Santa Ana Coastal Basins Due to
 Groundwater Withdrawal. *Water Resources Research*, *54*(5), 3557–3582. doi:
 799 10.1029/2017WR021978
 800
 801 Roberts, S., & Everson, R. (Eds.). (2001). *Independent Component Analysis*. Cam-
 bridge University Press. doi: 10.1017/CBO9780511624148
 802
 803 Serpelloni, E., Pintori, F., Gualandi, A., Scocimarro, E., Cavaliere, A., Ander-
 804 lini, L., . . . Todesco, M. (2018). Hydrologically Induced Karst Deforma-
 tion: Insights From GPS Measurements in the Adria-Eurasia Plate Boundary

- 805 Zone. *Journal of Geophysical Research: Solid Earth*, 123(5), 4413–4430. doi:
 806 10.1002/2017JB015252
- 807 Shiklomanov, I. (1993). World fresh water resources. In P. H. Gleick (Ed.), *Water in*
 808 *crisis: A guide to the world's fresh water resources*. Oxford University Press.
- 809 Silverii, F., D'Agostino, N., Métois, M., Fiorillo, F., & Ventafridda, G. (2016, nov).
 810 Transient deformation of karst aquifers due to seasonal and multiyear groundwater
 811 variations observed by GPS in southern Apennines (Italy). *Journal of Geophysical*
 812 *Research: Solid Earth*, 121(11), 8315–8337. doi: 10.1002/2016JB013361
- 813 Tapley, B. D., Bettadpur, S., Ries, J. C., Thompson, P. F., & Watkins, M. M.
 814 (2004). Grace measurements of mass variability in the earth system. *Science*,
 815 305(5683), 503–505.
- 816 Tsai, V. C. (2011, apr). A model for seasonal changes in GPS positions and seismic
 817 wave speeds due to thermoelastic and hydrologic variations. *Journal of Geophysi-*
 818 *cal Research*, 116(B4), B04404. doi: 10.1029/2010JB008156
- 819 van Dam, T., Wahr, J., Milly, P. C. D., Shmakin, A. B., Blewitt, G., Lavallée, D.,
 820 & Larson, K. M. (2001). Crustal displacements due to continental water loading.
 821 *Geophysical Research Letters*, 28(4), 651–654. doi: 10.1029/2000GL012120
- 822 Vergnolle, M., Walpersdorf, A., Kostoglodov, V., Tregoning, P., Santiago, J., Cotte,
 823 N., & Franco, S. (2010). Slow slip events in Mexico revised from the processing of
 824 11 year GPS observations. *Journal of Geophysical Research: Solid Earth*, 115(B8).
- 825 Verruijt, A. (2009). Elastostatics of a Half Space. In *An introduction to soil dynam-*
 826 *ics*. doi: 10.1007/978-90-481-3441-0
- 827 Walsh, J. B. (1965). The effect of cracks on the compressibility of rock. *Journal of*
 828 *Geophysical Research (1896-1977)*, 70(2), 381–389. doi: [https://doi.org/10.1029/
 829 JZ070i002p00381](https://doi.org/10.1029/JZ070i002p00381)
- 830 Wang, H. F. (2000). *Theory of Linear Poroelasticity with Applications to Geome-*
 831 *chanics and Hydrogeology*. Princeton University Press.
- 832 Westerman, D. A., Gillip, J. A., Richards, J. M., Hays, P. D., & Clark, B. R. (2016).
 833 Altitudes and thicknesses of hydrogeologic units of the Ozark Plateaus aquifer sys-
 834 tem in Arkansas, Kansas, Missouri, and Oklahoma. *U.S. Geological Survey Scientific*
 835 *Investigations Report*(2016-5130), 32.
- 836 Wisely, B. A., & Schmidt, D. (2010, 3). Deciphering vertical deformation and
 837 poroelastic parameters in a tectonically active fault-bound aquifer using InSAR
 838 and well level data, San Bernardino basin, California. *Geophysical Journal In-*
 839 *ternational*, 181, 1185–1200. Retrieved from [https://academic.oup.com/
 840 gji/article-lookup/doi/10.1111/j.1365-246X.2010.04568.x](https://academic.oup.com/gji/article-lookup/doi/10.1111/j.1365-246X.2010.04568.x) doi:
 841 10.1111/j.1365-246X.2010.04568.x